BioSystems 145 (2016) 53–66

Contents lists available at ScienceDirect

BioSystems

journal homepage: www.elsevier.com/locate/biosystems

On the importance of modelling the internal spatial dynamics of biological cells

Faiz Sayyid, Sara Kalvala*

Department of Computer Science, University of Warwick, Coventry, West Midlands, United Kingdom

ARTICLE INFO

Article history:
Received 15 July 2015
Received in revised form 25 May 2016
Accepted 31 May 2016
Available online 2 June 2016

Keywords:
Whole-cell simulation
Reaction–diffusion
GPGPU
Single-cell dynamics

ABSTRACT

Spatial effects such as cell shape have very often been considered negligible in models of cellular pathways, and many existing simulation infrastructures do not take such effects into consideration. Recent experimental results are reversing this judgement by showing that very small spatial variations *can* make a big difference in the fate of a cell. This is particularly the case when considering eukaryotic cells, which have a complex physical structure and many subtle control mechanisms, but bacteria are also interesting for the huge variation in shape both between species and in different phases of their lifecycle.

In this work we perform simulations that measure the effect of three common bacterial shapes on the behaviour of model cellular pathways. To perform these experiments we develop ReDi-Cell, a highly scalable GPGPU cell simulation infrastructure for the modelling of cellular pathways in spatially detailed environments. ReDi-Cell is validated against known-good simulations, prior to its use in new work. We then use ReDi-Cell to conduct novel experiments that demonstrate the effect that three common bacterial shapes (*Cocci*, *Bacilli* and *Spirilli*) have on the behaviour of model cellular pathways. Pathway wavefront shape, pathway concentration gradients, and chemical species distribution are measured in the three different shapes. We also quantify the impact of internal cellular clutter on the same pathways. Through this work we show that variations in the shape or configuration of these common cell shapes alter model cell behaviour.

1. Introduction

The intricate networks of complementary physiological processes that compose cellular behaviour have been modelled in a number of studies (Loew and Schaff, 2001; Karr et al., 2012). These processes are broadly known as cellular pathways. Some of this modelling is reaction-only (Orton et al., 2005; Gong et al., 2010; den Breems et al., 2014) and thus is not able to simulate the spatially heterogeneous nature of the cell. Whilst reaction-only models of cellular pathways have provided great insight there is scope to improve the representation of the cell by capturing the cell environment's spatial details, such as cell geometry and organelle placement. Further work is required to understand the influence of spatial organisation on cellular processes (Kholodenko, 2009). Reaction–diffusion systems can extend these reaction only models by allowing the chemical species and organelles to be accurately positioned in the cytoplasm and by permitting the virtual cell to take its natural shape. *In silico* studies allow a degree of measurement and control that is impossible *in vitro*.

In this work we simulate the effect of cell shape and organelle placement on abstracted cellular pathways modelled by reaction–diffusion systems (Sections 3 and 4). While the simulations performed in this work are computationally expensive, the numerical methods chosen are inherently suited to massively parallel hardware such as a GPU.

We develop ReDi-Cell (Section 5), a performant and scalable GPGPU cell simulation environment suitable for this work. ReDi-Cell is validated against VCell, a known-good cell simulation (Sections 6.1–6.3). While VCell would allow us to perform the same experiments as those undertaken in this work they would take much longer to perform due to VCell's inability to run on a GPGPU. In the validation experiments performed in this work we find that ReDi-Cell is approximately 24× faster than VCell. VCell is also closed source, making it impossible to port it to any other architecture.

We then perform novel experiments that examine the effect that three common cell shapes (*Cocci*, *Bacilli* and *Spirilli*) have on model

Abbreviations: ReDi-Cell, reaction–diffusion cell; GPGPU, general purpose computing on graphical processing units.

* Corresponding author.
E-mail addresses: f.sayyid@warwick.ac.uk (F. Sayyid), s.kalvala@warwick.ac.uk (S. Kalvala).

http://dx.doi.org/10.1016/j.biosystems.2016.05.012

cellular pathways. Pathway wavefront shape, pathway concentration gradients, and chemical species distribution are measured in three different shapes in order to quantify spatial sensitivity (Sections 6.5 and 6.6). Finally, the dampening potential of clutter on intracellular signalling pathways is explored (Section 6.7).

By performing these simulations we seek to quantify the effect of three common cell shapes, and internal clutter on the dynamics of virtual cellular pathways. Numerical simulation allows us to answer these questions when it would be challenging to find closed form analytical solutions.

2. Background

In this section we review the related biological background for this work. Cellular dynamics and the evidence (both experimental and theoretical) for their spatially sensitive nature are discussed in detail.

2.1. Cellular dynamics

Cells receive and process signals related to internal and external changes in the environment, such as infection, stress, injury, or nutrient need. This behaviour is achieved through mechanisms known as biological pathways, a series of internal molecular interactions that lead to a specific change in the cell. The effects of these interactions vary widely, but can include the production of a new chemical species, such as a fat or a protein, or generating cell movement.

Most cellular pathways fall into one of two categories: metabolic, or signal transduction. Metabolic pathways involve the transformation of one species into another, either to be used immediately, to be stored, or to initiate other metabolic pathways. Signal transduction pathways amplify extracellular signals received at surface receptors and propagate them through the cell. Cellular behaviour is also controlled by gene regulatory networks, which are responsible for turning genes on and off. This switching governs the production of proteins.

It has become clear that these reaction pathways are highly spatially organized within the cell, with many reactions occurring only in specific regions (Srere, 2000). For example, within signal transduction pathways, spatial gradients and microdomains of signalling occur due to localised chemical species, such as phosphatases. As intracellular distances increase, active signalling messengers are more likely to become deactivated on their journey to the cell interior (Meyers et al., 2006). The dose response curves of the yeast Mitogen Activated Protein Kinase (MAPK) cascade differ depending upon both the geometry of the cell and the subtle change in feedback parameters (Zhao et al., 2011).

2.2. Examples of spatially sensitive systems

Spatially dependent behaviours, including pathway dynamics, have been documented in both computational and experimental studies. Flourescence resonance energy transfer-based technologies have been used to find concentration gradients and have given experimental proof of spatially sensitive processes (Meyers, 2012). Concentration gradients have been found to exist in a number of systems including phosphorylated stathmin/oncoprotein 18 (Niethammer et al., 2004), MAPK Fus3 (Maeder et al., 2007), and Aurora B kinase (Fuller et al., 2008).

Some cellular processes cannot take place without the existence of concentration gradients. The propagation of an action potential along the axon is an extreme example of a system dependent on concentration gradients. As the potential moves along the axon, spatial gradients in membrane potential and currents are formed. The interaction between the gradients and the ion channels continue to force the wave along the axon. The behaviour of this system is intrinsically spatially dependant, and nonspatial models might fail to capture the propagation.

Calcium wave and spark models are another example of a system that is spatially sensitive. Calcium waves are necessary for the continuation of development in some eggs after fertilization. Recent experimental and theoretical work suggests that calcium wave propagation may be affected by the positioning of intracellular calcium release channels (Chen et al., 2014). *In silico* Myocyte behaviour has also been demonstrated to depend on spatial organisation (Weng et al., 1999). Spatial models have given us the first mechanistic insights, showing micro-domain dynamics to be a system level property arising from the complex interacting behaviour of the cell (Neves and Iyengar, 2009).

The translocation of Nuclear Factor κB (or NF-κB) in tumor cells is also spatially sensitive. It has been demonstrated experimentally that cell shape and micro-environmental factors regulate the translocation of NF-κB, which may in turn play a key role in the development and therefore potentially the treatment of some forms of cancer (Dolcet et al., 2005).

2.3. Mechanisms for spatial sensitivity

It is established in Section 2.2 that many cellular processes are spatially sensitive. In order to model these spatially sensitive systems in an appropriate way we review which major physical properties of the cell environment cause this sensitivity.

2.3.1. Concentration gradients

Some models of cell biology implicitly assume that chemical species concentrations are homogeneously distributed across space (Orton et al., 2005; Gong et al., 2010; den Breems et al., 2014). However when the reaction space becomes relatively large and chemically connected to other systems, concentrations may become heterogeneous, giving rise to concentration gradients. It has become clear that these spatial gradients exist in a wide range of cellular processes (Howard, 2006).

In addition to reactant locality, *reaction* locality, such as activation at the membrane and deactivation in the cytoplasm, gives rise to concentration gradients. If one reaction depends on chemicals produced at two different locations then those two chemicals must diffuse to the reaction site for the reaction to occur. As the concentration of the diffusing chemical is less at the reaction site than at the production site, a gradient is formed. In some cases concentration gradients can be attributed to the different diffusivities of the same protein in active and inactive forms (Kholodenko, 2009). Concentration gradients change reaction system dynamics. Nonspatial models make the simplifying assumption that concentration is uniform through the cell and therefore might predict incorrect values of the diffusing chemical.

2.3.2. Cell shape

Living cells take on a variety of different sizes and shapes leading to different surface-to-volume ratios and intracellular distances. The shape of the cell has been found to affect cellular process dynamics (Soh et al., 2010). Cells without uniform shape have been shown to alter reaction pathways in interesting ways; the neuron axon is an extreme example, dendrites and soma all exhibit geometry that can lead to chemical reactions preferentially occurring in different parts of the cell (Meyers et al., 2006; Kholodenko and Kolch, 2008). This may cause different travel times for the same chemical at different phases in the cell's life cycle, as the cell grows. If a change in travel time for a particular chemical is not accounted for, chemical gradients predicted by the model may be incorrect.

2.3.3. Cellular sub-structure

The geometry and position of substructures within the cell can play an important role in the spatial restriction of chemical reactions and hence physiological processes. Some chemical processes are only able to take place within specific organelles. For example, organelles such as endosomes and the Golgi apparatus play a critical role in regulating signal transmission to the nucleus (Hwang et al., 2014). Precise positioning of these organelles within the cell is of central importance to effective cell regulation (Hwang et al., 2014). It follows that accurate representation of organelle position and geometry is necessary for the correctness of an *in silico* experiment.

3. Spatial mathematical models of cellular systems

Having established the importance of spatial organisation in cellular systems we now review mathematical models capable of representing the heterogeneous nature of the cell environment.

3.1. Reaction–diffusion models

Reactions have been modelled by various techniques including ordinary differential equations (ODE) and stochastic processes. However diffusion, an intrinsic physical phenomenon sometimes remains neglected. The aforementioned spatial factors (Section 2) would not be important if chemicals did not move. Reaction–diffusion models extend the basic reaction model by adding a diffusive transport system that represents the movement of chemicals.

Some cells have evolved to take advantage of diffusion's low energy requirement for chemical transport (Soh et al., 2010). It is important to note that when the diffusion process is much faster than the reaction process the effect of diffusion on the dynamics of the system is decreased. In these cases reaction-only systems may be sufficient. We therefore limit discussions of reaction–diffusion systems to those in which both reaction and diffusion have a significant impact on the dynamics of the system. Due to high chemical concentrations, metabolic pathways such as glycolysis rely on diffusion as a means of transport across the cytoplasm. In addition, any process involving cytoplasmic/nuclear shuttling may also be affected by diffusion.

Reaction–diffusion systems can model complex chemical configurations which are impossible with reaction-only systems. A system of reacting and diffusing chemicals can thus evolve from an initial, relatively uniform state to a complex state (Turing, 1990). For example, Gray–Scott systems have been shown to be capable of mimicking biological pattern formation (Maini et al., 1997).

Such studies demonstrate that reaction–diffusion systems are intrinsically spatial and so they are well suited to modelling the arbitrarily shaped boundaries of *in silico* representations of cells. The ability to vary the diffusion coefficients in reaction–diffusion models can be used to computationally identify parameters that are likely to reproduce experimentally observed microdomain behaviour.

There are many different ways to construct a reaction–diffusion system. A reaction–diffusion model can be formulated by adding a diffusive component to an already tested reaction model. The three most common reaction systems are the Stochastic Simulation Algorithm (SSA), the Chemical Langevine Equation (CLE) and the Reaction Rate Equation (RRE). The SSA can be made spatial by discretising the reacting space and treating a diffusive event, from one spatial quanta to another, as a reaction (Erban et al., 2016). The CLE can be modified by adding a term for white Gaussian noise to simulate diffusion (Andrews et al., 2009). The RRE is subject to perhaps the most recognisable modification; by incorporating Fick's law of diffusion RRE systems become Partial Differential Equation-Ordinary Differential Equation (PDE-ODE) hybrid systems.

Finally, there exist particle based reaction–diffusion models. These systems represent particles explicitly, with physical laws, such as Molecular Dynamics (MD) or Brownian Dynamics (BD) (Plimpton and Slepoy, 2005) (or approximations thereof) dictating the evolution of the system.

3.2. PDE based reaction–diffusion models

PDE-ODE based reaction–diffusion systems are a suitable technique to simulate reaction–diffusion models inside cells (Neves and Iyengar, 2009). PDE-ODE reaction–diffusion models allow the formation of spatial gradients by permitting the localisation of chemical species and the description of cell substructure morphology within easily expressible boundary conditions.

As the PDE-ODE model extends the ODE model, comparisons are often made between the two; ODEs describe the change in concentration of a set of species over time, whereas PDE-ODE models describe the change in concentration of a set of species over time and space (Eungdamrong and Iyengar, 2004). PDE-ODE models take account of the diffusive processes that occur within a system as well as changes in concentration due to reaction. Mathematically, we describe a PDE-ODE reaction–diffusion system as:

$$\frac{\partial u}{\partial t} = D\nabla^2 u + R(u) \tag{1}$$

or alternatively:

$$\frac{\partial u}{\partial t} = D\left(\frac{\partial^2 u}{\partial x^2} + \frac{\partial^2 u}{\partial y^2} + \frac{\partial^2 u}{\partial z^2}\right) + R(u) \tag{2}$$

where u is the concentration, D is the diffusion coefficient and R is a system of reactions described by a set of ODEs. The PDEs (∇u) and ODEs ($R(u)$) require different solving techniques.

In real systems there can be many different chemical species. As the number of species and the number of reactions increases the computational cost for solving the PDE-ODE reaction–diffusion equation also increases. This is due to the increase in the number of terms in $R(u)$ and the number of times the PDE equation is solved. PDE reaction–diffusion simulations (like all other reaction–diffusion simulation techniques) are not without their drawbacks, requiring diffusion coefficients and initial reactant concentrations, and locations, which are sometimes unknown. Theoretical diffusion coefficients can be calculated from molecular weights and, with the advent of fluorescence recovery after photobleaching experiments, it is possible to directly measure the diffusion coefficients of cellular components.

3.3. Solving PDE-ODE reaction–diffusion models

Eq. (1) has both an ODE component and a PDE component. In this section we describe methods for computationally solving these two types of differential equation. Hyperbolic PDEs such as the diffusion equation can be solved in many different ways. Two of the most common are the explicit finite difference method (FDM) and the implicit Crank–Nicholson method. FDM is bound by the condition that $\Delta t/\Delta x^2 < 0.5$ (Smith, 1985); that is, the size of the time step (Δt) divided by the square of the smallest measurable distance (Δx) must be less than 0.5.

The choice of Δx is important as it dictates the level of detail that can be extracted from our simulation. If one wanted to model a cellular process at the level of an organelle, then dx would need to be at least as small as the smallest dimension of the organelle in question. The explicit condition would then require that the time step be made even smaller, which increases runtime of the simulation.

The alternative to using an explicit scheme is an implicit scheme, where the reaction–diffusion system is solved as a set of simultaneous equations by a linear solver. Implicit methods do not have to observe the same time/space ratio requirement, however it is more challenging to implement boundary conditions (such as complex cell and organelle shapes) in an implicit regime.

ODE systems, such as the RRE component of the reaction–diffusion equation, have enjoyed utility across a range of disciplines and as such many robust solving techniques exist. Most numerical methods for solving ODEs approximate the solution by numerical integration. Reaction–diffusion systems generally take the form of first-order initial value problems (IVP). These can readily be solved using Runge–Kutta (RK) methods.

3.4. Summary

We have seen in the literature that a wide variety of cellular processes are affected by cell shape, organelle placement and initial concentration of chemical species. It is also seen that reaction–diffusion systems can accurately model these processes' spatial dynamics.

4. A representative abstraction for cellular pathways

Cellular pathways can involve large numbers of chemical species taking part in complex networks of chemical reactions. Often, initial conditions and parameters in these networks are unknown. In this work we are not interested in a specific reaction system, only the effect of the cell environment on a *general* reaction system. Fundamentally all cell processes are chemical, therefore we can model any physiological process (at an abstract level) with a general reaction system coupled with diffusion. Therefore we simulate *abstracted* cellular pathways that obviate the need for unknown parameters, yet are representative of a simple cellular pathway. We select the Lotka–Volterra (Lotka, 1925; Volterra, 1927) (LV) reaction model as the abstraction.

The LV model was independently proposed to explain two different behaviours; the increase in the number of predatory fish in the Adriatic and a theoretical, oscillating, chemical reaction. The model is the simplest example of a predator-prey system (McLaughlin and Roughgarden, 1991) and its properties have been widely studied in the literature. In a predator-prey system, agents compete with each other and the environment to survive. In general, predator-prey systems describe *competitive interactions*. The nature of the agents vary by application but commonly take the form of carnivores and herbivores, or as in this case chemical species.

The LV system is described as:

$$\frac{dx}{dt} = x(\alpha - \beta * y) \tag{3}$$

$$\frac{dy}{dt} = -y(\gamma - \delta * x) \tag{4}$$

where x is the number of prey, y is the number of predators, dx/dt and dy/dt are the rates of growth of the populations. α, β, γ, δ are parameters describing the interactions of the two species.

LV systems have previously been coupled with diffusion (LVD) (Hastings, 1978). Such investigations are normally concerned with the mathematical properties of the system, such as existence of solutions or stability analysis, rather than simulation or application. LVD simulations have occasionally been used to model ecological migration; putting the LV system back in its traditional setting. An example of such a study can be seen in (Modelica, 2014).

If it is found that the spatial organisation of the virtual cell alters the dynamics of a simple model cellular pathway (LVD), then it is highly likely that more complex pathways will have more pronounced effects.

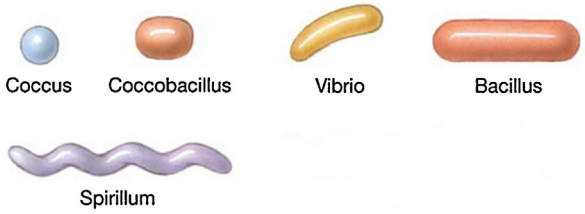

Fig. 1. Common bacterial shapes reproduced from (Bacterial Shapes, 2014).

5. ReDi-Cell

In Section 2 we saw that the cells display heterogeneous internal and external geometries, and that accurate representation of cell structure is crucial to simulation. Section 3 demonstrates that whilst computationally expensive, reaction–diffusion systems are highly suited to modelling cellular pathways in complex geometries. Finally Section 4 demonstrates that if we are interested in the effect of cell geometry on a *general* reaction system that complex pathways can be replaced with abstractions, such as the LVD system.

These conclusions suggest that cellular pathways simulations should be capable of representing abstractions of reaction–diffusion systems inside complex cell geometry in a performant manner. In this section we present ReDi-Cell, a novel simulation package that fulfils these requirements. The software is available at http://github.com/FaizSayyid/ReDi-Cell.

5.1. Description

ReDi-Cell is a 3D high performance GPGPU reaction–diffusion simulation of arbitrary cellular geometry. It is the first GPGPU PDE-ODE cell simulation infrastructure specifically designed for investigating the effect of realistic cell shapes and internal components. ReDi-Cell is designed to take cellular morphology information, store it as voxels, and numerically solve a reaction–diffusion system representing a physiological processes. Each voxel represents a quanta on a regularly spaced, three-dimensional grid.

Systems incorporating PDEs are more challenging to implement, with few large scale projects available for use (Neves and Iyengar, 2009). VCell (Loew and Schaff, 2001) is one such simulation package. VCell includes a variety of simulation techniques not limited to PDE simulation and has been used in a variety of published models.

ReDi-Cell, as a high performance GPGPU solver tailor made for PDE-ODE systems, scales to far more detailed problems over more time steps than are feasible with the available VCell interface. The user may dedicate as many GPUs as they have available to the task; spatial decomposition occurs over all available GPUs.

5.2. Realistic cell shapes

Cells and organelles appear in nature in a variety of shapes, as shown in Fig. 1. ReDi-Cell simulates these bacterial shapes by discretising arbitrary cellular morphology, described as 3D models, into voxels. Fig. 2 demonstrates how geometric primitives have been used to create 3D models to approximate three of the common cell shapes in Fig. 1. Where shapes cannot be described exactly by a single primitive, composites are formed. For example, *Bacilli* are best approximated by capsules; they can be built as a composite of a cylinder and two hemispheres.

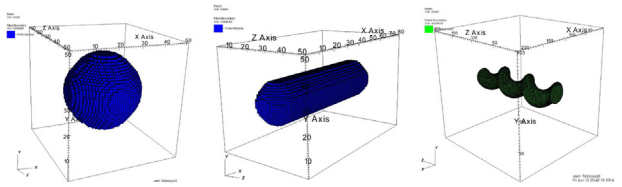

(a) *The Coccus* (b) *The Bacillus* (c) *The Spirillum*

Fig. 2. Approximations to cell shapes in Fig. 1 using the ViSiT software toolkit.

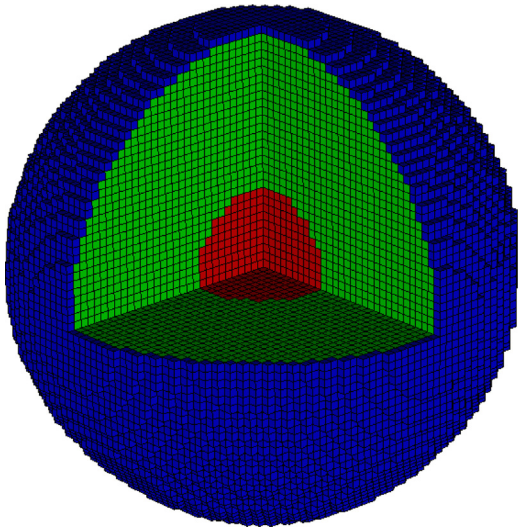

Fig. 3. Cutaway of a ReDi-Cell model *Coccus* showing the membrane, cytoplasm and nucleus produced using VisIt. The different colours represent different biological material types which have different simulation properties. These simulation properties allow for differing rates of reaction and diffusion in those areas of the cell.

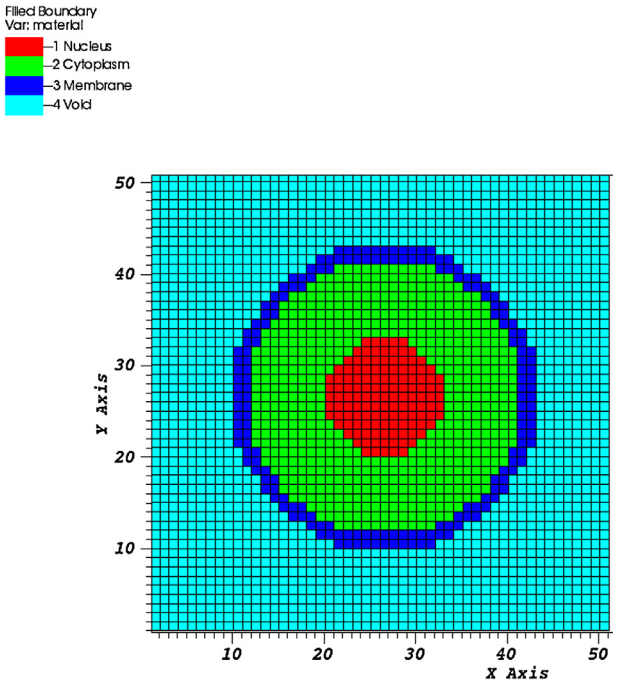

Fig. 4. 2D slice through the centre of the ReDi-Cell model of a *Coccus* depicted in Fig. 3. This figure illustrates the way in which VisIt can change perspective to show specific regions of interest. 2D slice results are used extensively in this work.

5.3. Cellular sub-components

ReDi-Cell allows internal cell components, such as organelles, to be represented. Each component's permeability can be altered by changing the diffusion parameter in that location in the cell. This allows ReDi-Cell components to mimic their biological analogues in the cell, with different reagents having different responses to different cell materials. For instance, some reagents are confined to the plasma membrane, where as others might be able to pass through. In Fig. 5 we see a chemical diffusing in a crowded cellular environment with cellular sub-components. The chemical, incapable of diffusing through the impermeable membrane of the cell nucleus is forced to diffuse around the clutter that represents an organelle. Fig. 3 shows an "onion-peel" decomposition of an example simulation environment. This illustrates the way ReDi-Cell components are capable of capturing the internal structure of the cell. Fig. 4 shows an example of a 2D slice through the same ReDi-Cell environment. Fig. 4 includes grid lines to show the way in which space has been discretised. The level of discretisation is configurable.

It is unlikely that all sub-cellular structures will have homogeneous morphology; organelles are of many different shapes and sizes. ReDi-Cell allows internal cell component shapes to be represented as accurately as the external cell shape. We see an example of this capability in Fig. 6, which shows spherical and cylindrical shaped organelles inside a *Spirillum*.

5.4. Simulation

Simulation execution in ReDi-Cell is divided into time steps. A single time step consists of a diffusion process and a reaction process. First, the ODEs representing the reactions are solved. This process occurs over each part of the cell in which diffusion is allowed to take place. Then the 3D PDE diffusion equation is solved for each reagent, again in the appropriate parts of the cell.

There are many different ways of solving PDEs and ODEs, as discussed in Section 3.3. We choose to solve PDEs using an explicit FDM algorithm (Smith, 1985) and ODEs using a Runge–Kutta 4 (RK4) algorithm (Press et al., 2002). The FDM algorithm is a common method of simulating reaction–diffusion and is used in many modern studies of such systems (Blagodatski et al., 2015). RK4 is an equally popular method of solving ODEs and despite enjoying less success on stiff systems is suitable for all of the systems that we use in this work. We show this to be true by verifying all simulated reaction systems against MATLAB's explicit ode45 solver. Matlab documentation suggests that if ode45 solves the system promptly then the system is not stiff (Matlab, 2016). In addition to this we verify our results against Mathematica's Wolfram Alpha ODE solver and it is once again demonstrated that a non-stiff solver is suitable for the systems used in this work.

ReDi-Cell uses *Visualise It* (VisIt) for visualisation, a popular open source tool for visualizing and analyzing data (Childs et al., 2012). VisIt is capable of displaying 2D slices of 3D shapes. In Figs. 4 and 6 we see examples of such cutaway cells. ReDi-Cell has two different implementations of the reaction–diffusion process, a parallel algorithm executed on the GPU and a serial algorithm executed on the CPU for when a compatible GPU is not available.

5.5. Implementation

Reaction–diffusion simulation methods (including the explicit FDM and RK4 algorithms implemented in ReDi-Cell) are extremely resource intensive. High performance computing architectures, such as the GPGPU targeted Nvidia CUDA (CUDA, 2014), enable the parallelisation of simulations, allowing faster run times and more detailed models. ReDi-Cell includes a CUDA GPU implementation of

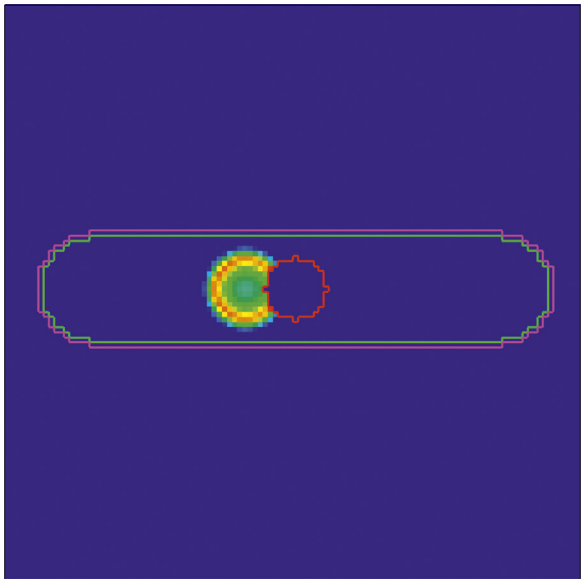

Fig. 5. 2D slice, produced using VisIt, through the centre of a ReDi-Cell model of a *Bacillus*, with a model chemical diffusing around a central organelle. This image shows how different materials can have different simulation properties and how VisIt can render materials in different ways. Instead of the solid material representations found in Fig. 4 and Fig. 3 only the boundaries of materials are drawn allowing both material type *and* chemical concentration to be rendered in the same image. The boundaries of the different biological materials are represented by the different coloured lines. Red represents the boundary of a central organelle, light green line the internal boundary of the cell and purple the external boundary of the cell. The boundaries in the image are overlayed on to a heatmap of chemical concentration, this is the reason that most of the image is dark blue (representing 0 concentration). The multi-coloured circle to the left of the central organelle shows the only non-zero concentration portion of the heatmap; a reacting and diffusing circle of chemical concentration that has not reached the internal boundary. At $t=0$ this chemical was a single point of concentration. The different materials have different simulation properties as discussed in Fig. 3. In this case the material enclosed by the red boundary does not permit reaction or diffusion to occur and the chemical is halted at the membrane. The membrane permits both reaction and diffusion but the rate of diffusion is halved. Beyond the purple line representing the external boundary of the membrane only diffusion processes are permitted. (For interpretation of reference to color in this figure legend, the reader is referred to the web version of this article.)

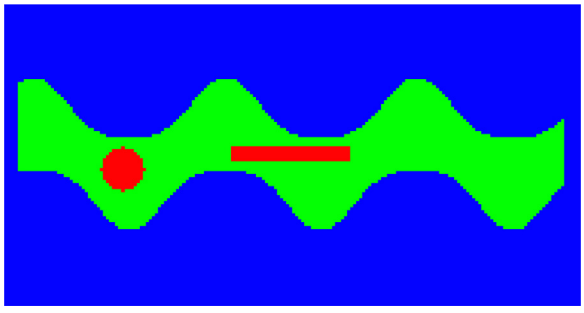

Fig. 6. 2D slice through the centre of a ReDi-Cell model *Spirillum* produced using VisIt. The boundaries in this image are solid as in Figs. 3 and 4 and so no concentrations are visible. This figure demonstrates different shaped organelles inside the model cell. Green represents the cytoplasm in which chemicals are permitted to react and diffuse. Red shapes represent organelles through which chemical cannot diffuse or react inside.

the Explicit FDM-RK4 reaction–diffusion method. In the GPU algorithm many reaction or diffusion events are run at the same time, instead of one after the other, as is the case in the CPU algorithm. In a single time step all reaction events are run after all diffusion events have taken place. During the simulation, data is written to the disk for offline analysis. Transferring data to and from the GPU is expensive and thus writing to disk every time step can degrade performance. Therefore we compromise, transferring data and writing to the disk at configurably sized intervals.

The execution of time steps is "batched" together in configurably sized intervals. Execution is paused between batches whilst results are written to the disk. The larger the batch size the faster the simulation will run. Time step batch sizes of 100 steps are commonly used, which provides a good trade-off between speed and output granularity.

The GPU algorithm has two stages: The kernel launcher, and the kernel itself. The kernel launcher runs on the CPU, it divides the simulation into batches and writes output to the disk. The kernel runs on the GPU and is responsible for executing the reaction process in parallel and then the diffusion processes in parallel across all of the GPU cores.

We also include a CPU algorithm. A single time step consists of a serial implementation of the explicit FDM-RK4 reaction–diffusion method. After each time step the state of the system is written to disk.

In terms of speed, we find that ReDi-Cell can perform faster than VCell. Using verification experiments 1 (Figs. 7 and 10(a)), 2 (Figs. 8 and 10(b)) and 3 (Figs. 9 and 10(c)) as benchmarks we find that ReDi-Cell is approximately 24× faster than VCell. ReDi-Cell benchmark simulations were performed on an NVIDIA Tesla K20.

Table 1
Description of validation experiments. The parameters used in the experiments are shown in the captions of the figures depicting experimental results.

System	Reaction equation	Initial conditions
Diffusion		A:10
$A+B\rightarrow C$	$\frac{dA}{dt}=-k*A*B$	A:10
	$\frac{dB}{dt}=-k*A*B$	B:10
	$\frac{dC}{dt}=k*A*B$	C:10

6. Experiments

In this section we detail three sets of experiments that we run with ReDi-Cell. The first is focused on validating ReDi-Cell's implementation against the state of the art, VCell. The validation experiments use two different prototypes: diffusion only and $A+B\rightarrow C$. A summary of the reaction systems is shown in Table 1. In the second set we investigate the behaviour of abstracted cellular pathways in different cell shapes. In the third set we investigate the impact of clutter on the same pathways. For a discussion of the choice of diffusion coefficients see Appendix C.

Experiments take place in a variety of cluttered and uncluttered environments. The results take the form of concentration heat maps and concentration against time graphs.

Graphs of concentration against time are used when studying the dynamics of a reaction in a single volume. Heatmaps are used when measuring the concentration in many volumes at once, at a single point in time. We exploit this property to measure the effect of space on the distribution of concentration. Many heatmaps recorded at sequential times can be stitched together into an animation to show the same information as a concentration graph, but for multiple volumes at once. Both concentration against time graphs and heatmaps are common in cell simulation, with VCell (against which we validate our results) using these measurements.

6.1. Uncluttered diffusion

This set of experiments investigates diffusion-only behaviour. The diffusion-only system from Table 1 is run in an

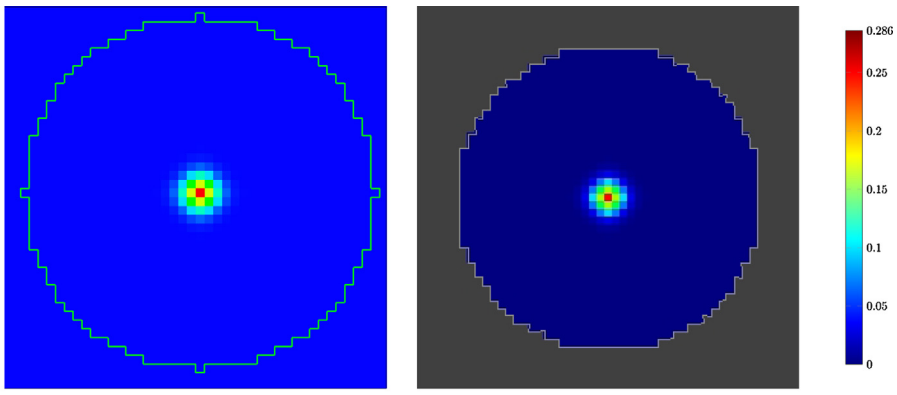

(a) Heat map of species A concentration in ReDi-Cell (b) Heat map of species A concentration in VCell

Fig. 7. Verification Experiment 1 – uncluttered diffusion. Heat maps of species A after 3000 time steps of diffusion. The experiment is run in both ReDi-Cell (Fig. 7(a)) and VCell (Fig. 7(b)). It can be seen that the heat maps are identical validating the accuracy of ReDi-Cell's diffusion computation. $k = 1.4^{12}$, $\Delta t = 10^{-14}$ s, $D = 1.0$, $\Delta x = 10^{-6}$ m.

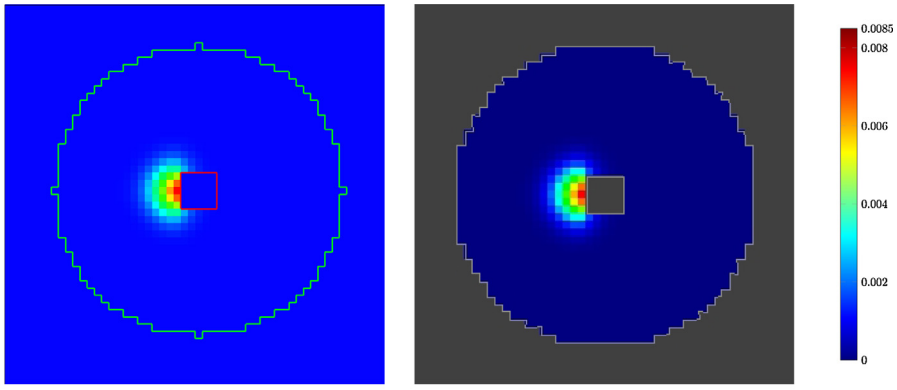

(a) Heat map of species concentration in ReDi-Cell (b) Heatmap of species concentration in VCell

Fig. 8. Verification Experiment 2 – cluttered diffusion. Heat maps of species A after 3000 time steps of diffusion. The experiment is run in both ReDi-Cell (Fig. 8(a)) and VCell (Fig. 8(b)). It can be seen that the heat maps are identical validating the accuracy of ReDi-Cell's cluttered diffusion computation. $k = 1.4^{12}$, $\Delta t = 10^{-14}$ s, $D = 1.0$, $\Delta x = 10^{-6}$ m.

uncluttered setting in ReDi-Cell. Results from this experiment are shown in Figs. 7(a) and 10(a). This same system was then run again in an identical uncluttered setting in VCell. Results from this experiment are shown in Figs. 7(b) and 10(a). These figures show that the results of these experiments are in good agreement.

6.2. Cluttered diffusion

This set of experiments examines how ReDi-Cell models the interaction of chemicals with the impermeable boundaries that model the internal cell wall and organelles. The diffusion system from Table 1 was run in a cluttered environment, consisting of a

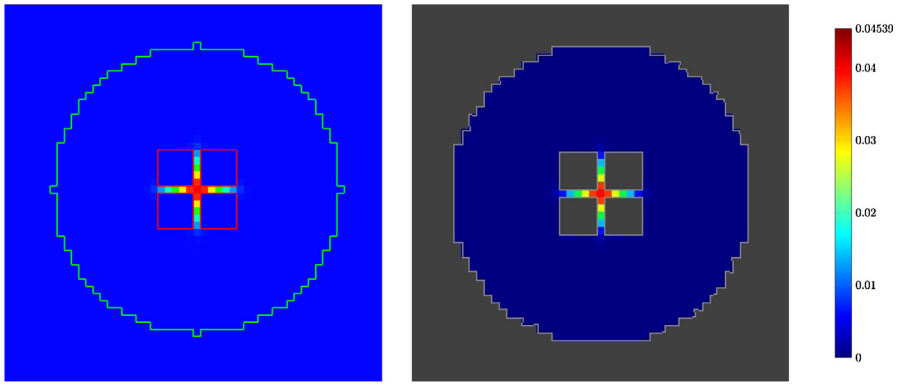

(a) Heatmap of species C concentration in ReDi-Cell (b) Heatmap of species C concentration in VCell

Fig. 9. Verification Experiment 3 – cluttered reaction–diffusion of the $A + B \rightarrow C$ system. The experiment is run in both ReDi-Cell (Fig. 9(a)) and VCell (Fig. 9(b)). It can be seen that the heat maps are identical validating the accuracy of ReDi-Cell's cluttered reaction–diffusion computation. $k = 1.4^{12}$, $\Delta t = 10^{-14}$ s, $D = 1.0$, $\Delta x = 10^{-6}$ m.

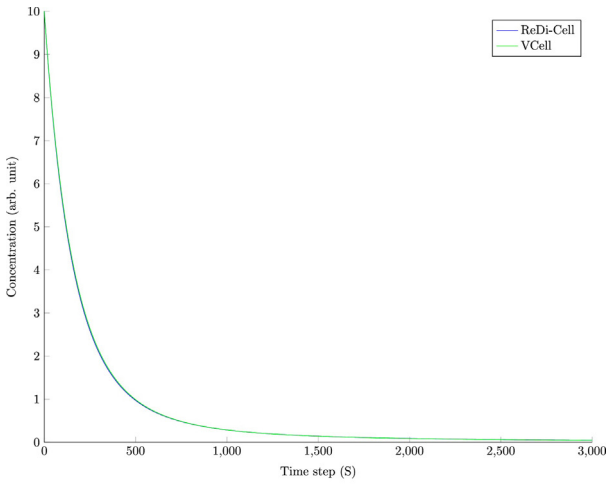

(a) Verification Experiment 1 - uncluttered diffusion.

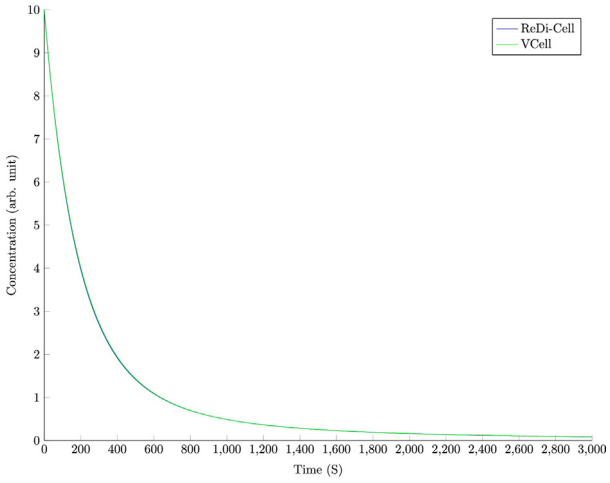

(b) Verification Experiment 2 - cluttered diffusion.

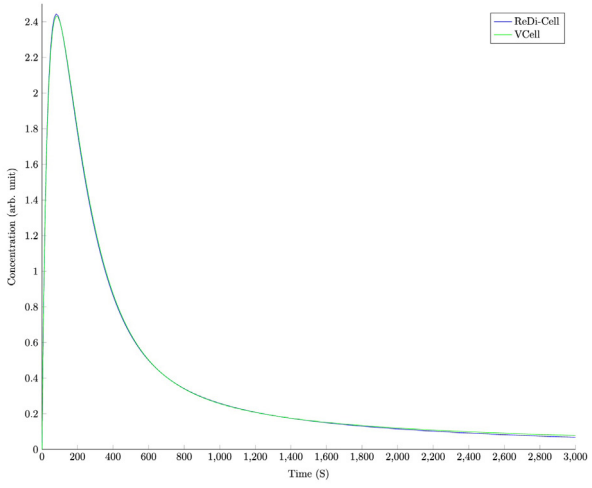

(c) Verification Experiment 3 - Cluttered reaction-diffusion of the $A + B \rightarrow C$ system.

Fig. 10. Graphs of species (A) concentration in ReDi-Cell and VCell measured in a single sub-volume over 3000 time steps. Concentration is measured in the sub-volume that the chemical was initially confined to. The lines that represent the concentration in ReDi-Cell and VCell are on top of each other validating the accuracy of ReDi-Cell's cluttered reaction–diffusion computation. $k = 1.4^{12}$, $\Delta t = 10^{-14}$ s, $D = 1.0$, $\Delta x = 10^{-6}$ m.

Table 2
Description of new work experiments. The parameters used in the experiments vary and so are shown in the captions of the figures depicting experimental results.

System	Reaction equation	Initial conditions
LVD	$\frac{dA}{dt} = A(\alpha - \beta * B)$	A:10
	$\frac{dB}{dt} = -B(\gamma - \delta * A)$	B:10

single impermeable cube. The species are initially located next to the cube. The experiment is first run in ReDi-Cell. Results from this experiment are shown in Figs. 8(a) and 10(b). The same system was run in VCell. VCell results are shown in Figs. 8(b) and 10(b). Once again, the results from ReDi-Cell and VCell are consistent with each other.

6.3. *Cluttered* A + B → C

In this set of experiments we investigate ReDi-Cell's behaviour when simulating reaction–diffusion next to impermeable membranes. The $A + B \rightarrow C$ reaction–diffusion system from Table 1 is run in a cluttered environment. This clutter takes the form of four impermeable cubes, separated by narrow channels. The species are initially located at the centre of the channels. The experiment is first run in ReDi-Cell, the results of this experiment are shown in Figs. 9(a) and 10(c). This experiment is run again in an identical environment in VCell. The results of this experiment are shown in Figs. 9(b) and 10(c). ReDi-Cell's results are shown to be consistent with VCell's.

Having validated ReDi-Cell against VCell we now use ReDi-Cell to perform novel experiments in Sections 6.5–6.7.

In all three sets of experiments run so far we find a good agreement between ReDi-Cell results and VCell results. The concentration trajectories for VCell and ReDi-Cell are nearly identical in all three experiments. Very little variation is shown between the two algorithms. Heat map results also show good agreement. The shapes of the ReDi-Cell and VCell concentration profiles in all three experiments show good agreements between each other. The values displayed in the heat map also show a very good agreement. In summary, it can be seen that ReDi-Cell is an accurate simulation of reaction–diffusion systems.

6.4. *The importance of spatial simulation*

Having discussed importance of spatial simulation we show the impact that removing spatial component has on a reaction–diffusion system. The system used in this experiment is the LVD system detailed in Table 2. To demonstrate this we run two experiments. In the first experiment we turn off diffusion allowing only reaction, thus making the experiment non spatial. In the second experiment we allow for both reaction and diffusion in a *Coccus*. The results of this experiment are shown in Fig. 11.

6.5. *LVD wavefronts in natural cell shapes*

This set of experiments measures the effect of cell shape on wavefront properties, specifically wavefront shape and wavefront concentration. We define the wavefront as the locus of points that are at the interface between zero and nonzero concentrations. The system used in this set of experiments is the LVD system detailed in Table 2.

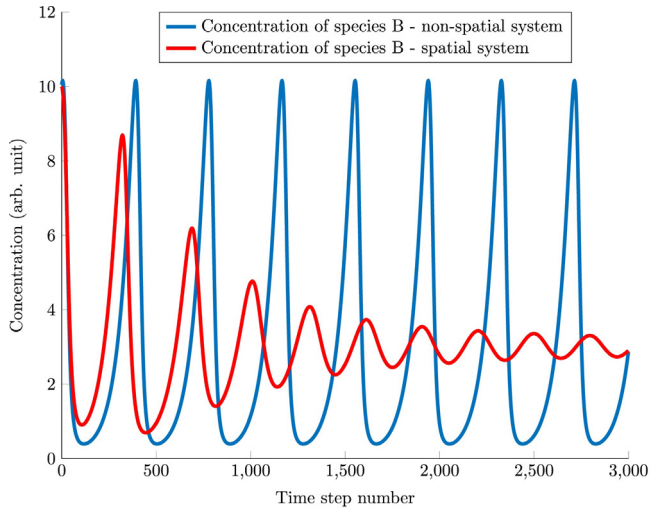

(a) Concentration of *Prey* species in the sub-volume that the chemical was initially confined to. $\alpha = 1.5 * 10^{12}$, $\beta = 1 * 10^{12}$, $\gamma = 3 * 10^{12}$, $\delta = 1 * 10^{12}$, *reaction rate* $= 10^{12}$

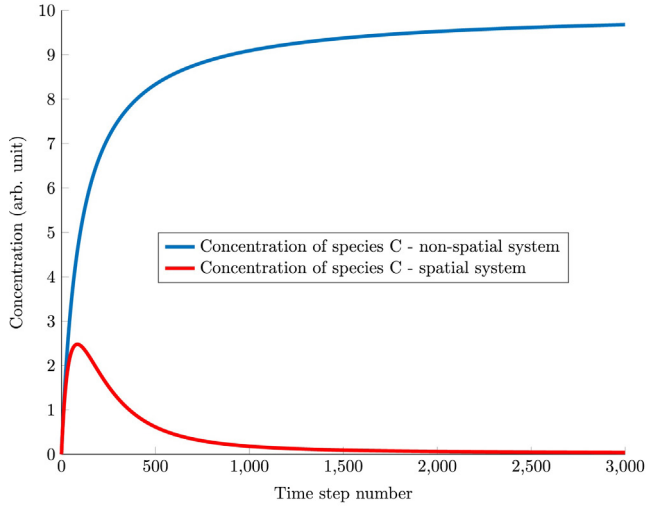

(b) Concentration of species C in the sub-volume that the chemical was initially confined to. $k = 1.4^{12}$

Fig. 11. A comparison of spatial and non spatial systems in ReDi-Cell. Concentration is measured in the sub-volume that the chemical was initially confined to. With both reaction systems it can be seen that there is a large difference in results between spatial and non-spatial systems. Both the final value of the concentration and the trajectory of the reaction over time vary substantially. Fixed parameters: $\Delta t = 10^{-14}$ s, $\Delta x = 10^{-6}$ m, $D = 0.02$.

Table 3
LVD wavefronts in natural cell shapes. Concentration at the wavefront after 1000 time steps. $\alpha = 1.5$, $\beta = 1.0$, $\gamma = 3.0$, $\delta = 1.0$, $\Delta t = 10^{-14}$ s, $\Delta x = 1.0 * 10^{-6}$ m, *reaction rate* $= 10^{12}$, $D = 1.0$.

Shape	Concentration at the wavefront
Coccus	1.06
Bacillus	1.38
Spirillum	2.61

The results of this set of experiments are shown in Fig. 12 and Table 3. The ReDi-Cell reaction vessels are approximations of real cell shapes. Three experiments were run, one in each cell shape. The volume, initial concentrations and initial positions of chemical species are kept analogous.

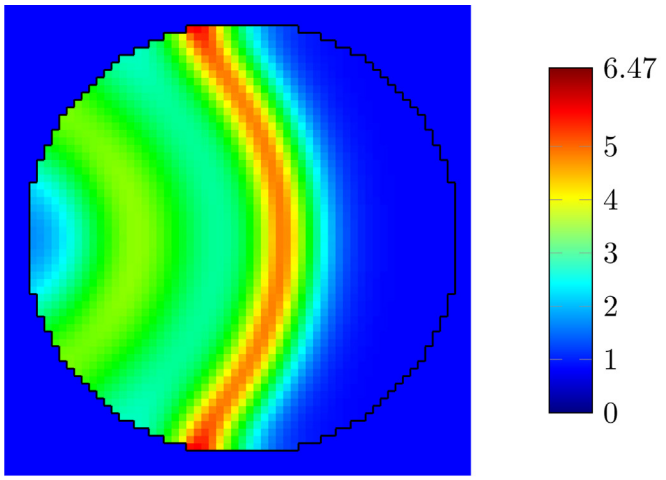

(a) Concentration of Species B in a *Coccus*

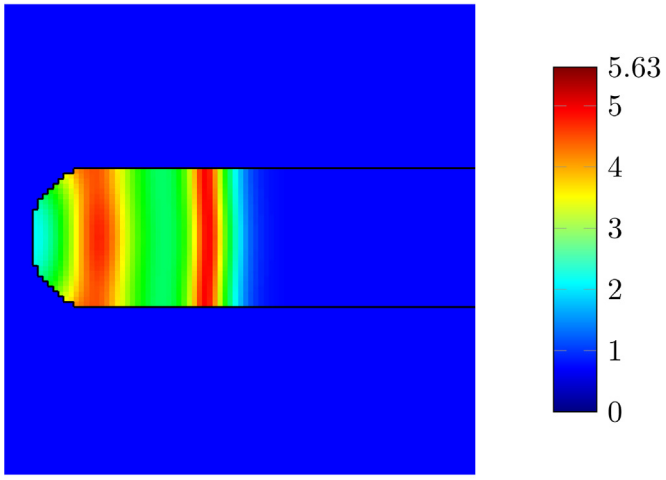

(b) Concentration of Species B in a *Bacillus*

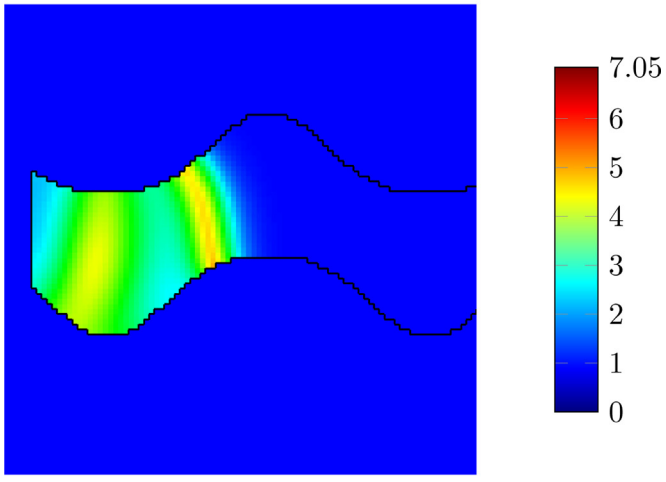

(c) Concentration of Species B in a *Spirillum*

Fig. 12. LVD wavefronts in natural cell shapes after 1000 time steps, simulated using ReDi-Cell and rendered in VisIt. In this figure we see the effect of running an LVD system in model natural cell shapes. $\alpha = 1.5$, $\beta = 1.0$, $\gamma = 3.0$, $\delta = 1.0$, $\Delta t = 10^{-14}$ s, $\Delta x = 1.0 * 10^{-6}$ m, *reaction rate* $= 10^{12}$, $D = 1.0$.

Table 4
Peak concentration after 2000 timesteps. $\alpha = 1.5$, $\beta = 1.0$, $\gamma = 3.0$, $\delta = 1.0$, $\Delta t = 10^{-14}$ s, $\Delta x = 1.0 * 10^{-6}$ m, *reaction rate* $= 10^{12}$, $D = 1.0$.

Shape	Peak concentration of species *A* after 2000 timesteps
Coccus	2.99
Bacillus	5.49
Spirillum	7.26

First, wavefront shape was investigated. The shape of the wavefronts are different in all three examples in Fig. 12. The *Coccus*' wavefront is extremely circular, whilst the *Bacillus*' wavefront is almost flat. The *Sprillum*'s wavefront, curves more steeply toward the bottom of the cell.

Next, we examine the effect that cell shape has on average wavefront concentration. The results are recorded in Table 3. The average concentration at the wavefront in all three bacterial shapes is different. The concentration gradients behind the wavefront are also different, for example whilst the concentration behind the wavefront in the *Bacillus* and in the *Coccus* are homogeneous, their values are different.

Different surface area to volume ratios may be responsible for the unique patterns of reflection inside virtual cells and so cause the difference in concentration gradients and wavefront shape between cell shapes seen in this section. In geometries with lines of symmetry, such as the *Coccus* and *Bacillus*, concentration waves are reflected in a uniform, symmetric fashion. The *Spirillum* is nonuniform in shape and thus reflections are not necessarily symmetric about the longest axis of the cell. This may produce the asymmetric wavefronts seen in the results. Changes in reflective properties may alter micro dynamics in equally distinct ways and so change the global response of the system. In addition, in cells of equivalent volume signals in the simulated *Coccus* travel a greater fraction of the cell's length.

6.6. LVD species distribution

This set of experiments examines the effect cell shape has on final species distribution. Species distribution is measured as follows. The 3D cell is divided into 2D slices along the cell's longest axis, with each slice having a thickness equal to one simulation unit length, Δx. The total amount of a given species in each slice is found by iterating over each sub-volume in the slice and summing the contributions. Finally the total amount of a particular species in each slice is plotted against the position of that slice along the cell.

The LVD system detailed in Table 2 is run in the three different cell shapes. The species distribution profile is recorded after 2500 timesteps. The species distributions are shown in Fig. 13 and the peak concentration are shown in Table 4.

We see several differences between the graphs in Fig. 13. Different cellular geometries result in different concentration profiles and peak concentrations. The shapes of the concentration profiles are different in each example. The *Coccus* has a more concentrated profile with the greatest peak concentration, the *Spirillum* has a mostly uniform profile with a lower peak, but the *Bacillus* shows the most difference. Discounting the tapering edge, we achieve a flat profile, with a spike at the wavefront.

6.7. LVD with cellular clutter

In this set of experiments we measure the effect of intra-cellular clutter on the dynamics of the LVD system. Two experiments were run, the initial conditions for which are shown in Fig. 14(a)

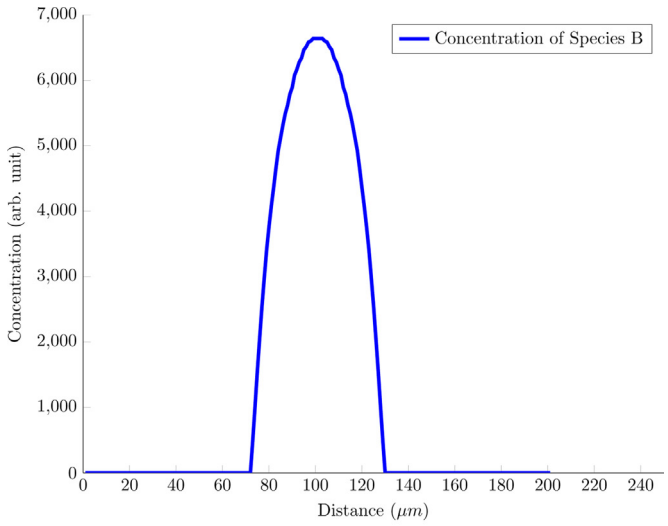

(a) Distribution of Species A in a *Coccus*

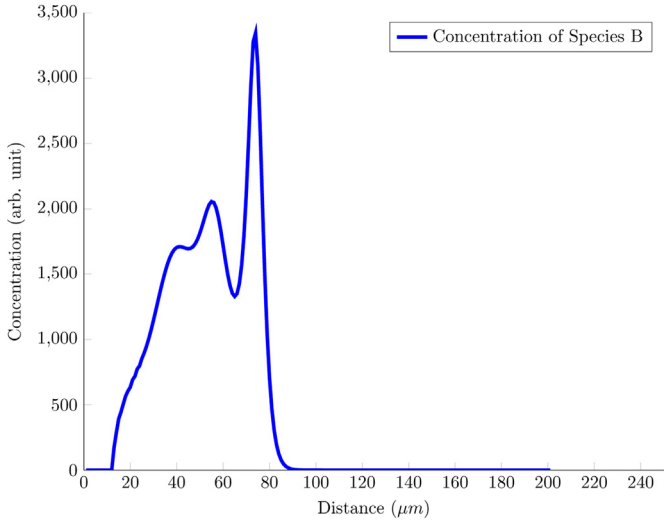

(b) Distribution of Species A in a *Bacillus*

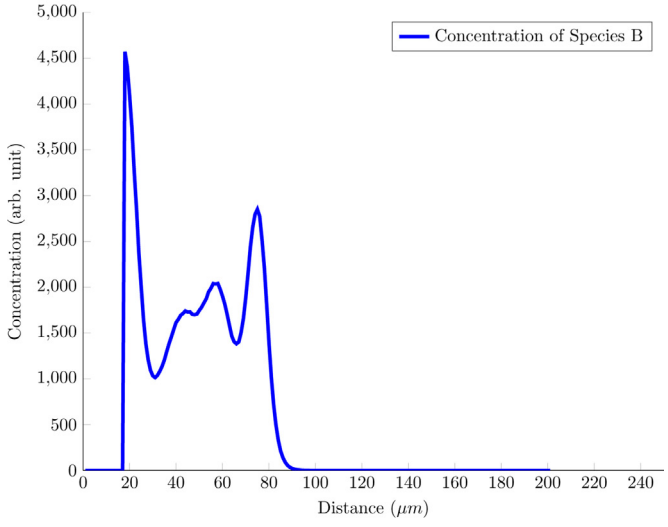

(c) Distribution of Species A in a *Spirillum*

Fig. 13. LVD concentration distribution after 1500 timesteps, simulated using ReDi-Cell and rendered in VisIt. $\alpha = 1.5$, $\beta = 1.0$, $\gamma = 3.0$, $\delta = 1.0$, $\Delta t = 10^{-14}$ s, $\Delta x = 1.0 * 10^{-6}$ m, *reaction rate* $= 10^{12}$, $D = 1.0$.

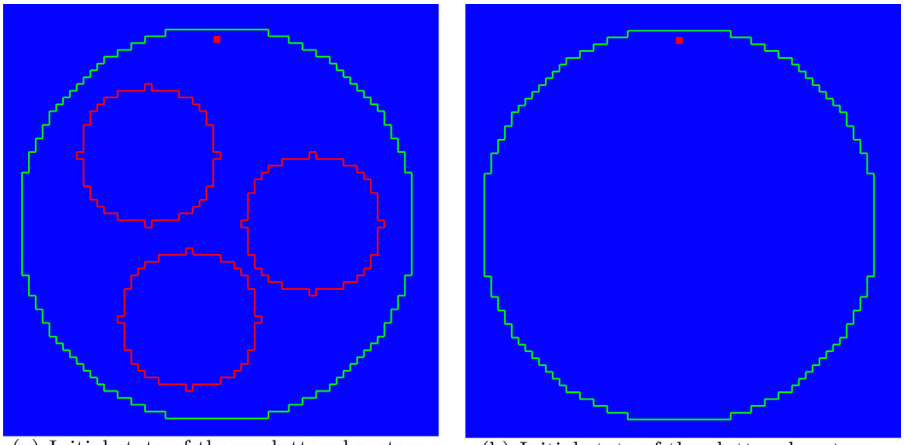

(a) Initial state of the uncluttered system. (b) Initial state of the cluttered system.

Fig. 14. LVD with cellular clutter. This figure shows the cluttered and uncluttered model cell initial conditions, rendered in VisIt. Measurement site is the small red square at the top.

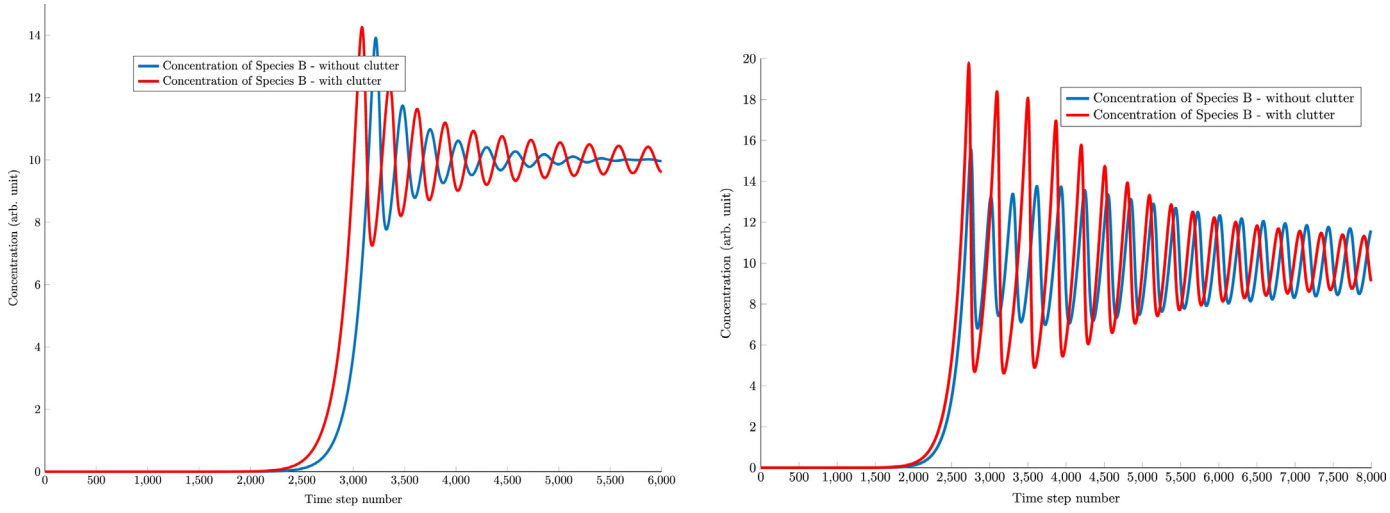

(a) $D = 1.0$ (b) $D = 0.5$

Fig. 15. LVD with cellular clutter. Species *A* concentration, in cluttered and uncluttered settings, measured over 4000 timesteps at the measurement site in the model cells as detailed in Fig. 14. This simulation was performed using ReDi-Cell. Fixed experimental parameters: $A = 1$, $B = 10$, $\alpha = 0.5$, $\beta = 1.0$, $\gamma = 10.0$, $\delta = 1.0$, $\Delta t = 10^{-14}$ s, $\Delta x = 1.0 * 10^{-6}$ m, *reaction rate* $= 10^{12}$.

(uncluttered system) and 14(b) (cluttered). The results are shown in Fig. 15(a). The only variable changed is the interior volume, by adding three spheres to represent clutter. The volume of the cell, the initial concentrations and initial positions of species *A* and species *B* are all kept constant in each experiment. Concentration is measured at the top of the virtual cell, this is location is marked by the red outlined square at the top of Fig. 14(a).

Fig. 15(a) shows the difference in cluttered and uncluttered environments on the arrival of species *A* at a location immediately next to the membrane and opposite to the source.

Clutter within virtual cells can change the way in which *in silico* biochemical processes progress by changing the flow of a chemical species through the system. Specifically, clutter has two impacts on this system: firstly, the time of arrival of species *A* is different, and secondly, the shape of the concentration profiles are different. The range of concentration values taken is much smaller. The signal has been damped by the clutter in the system. All of these factors contribute to the differences in concentration gradient between damped and undamped systems.

7. Conclusions and further work

We have performed simulations that show how the behaviour of model cellular pathways changes between three common cell shapes, and how the configuration of internal cellular clutter can alter the way in which signals propagate through a virtual cell. In doing so we show that model cellular pathways are sensitive to the shape and the internal geometry of the cell. We also showed which physical properties of the model pathway change when the cell shape changes; specifically, wavefront shape, peak concentration and concentration distribution are all affected by the shape of the cell. Finally, we have developed a novel GPGPU high performance cell simulation toolkit suitable for performing these experiments.

In theory VCell could have been used to perform the experiments in this work, albeit at a reduced speed. When benchmarked using the validation experiments it was found that ReDi-Cell performed approximately 24× faster than VCell. It may be possible to port VCell to the CUDA architecture used by ReDi-Cell, but as VCell is closed source it is impossible for an end user to do so. In

contrast ReDi-Cell is open source allowing users to change the source code to take advantage of any future developments in computing architecture. In addition the client/server nature of VCell means that jobs are scheduled before execution, possibly incurring an additional delay. Finally, ReDi-Cell uses the dedicated "VisIt" visualisation toolkit which enables results to be presented in a variety of ways not possible with the VCell viewer.

One issue in trying to model cellular phenomena in detail has been the lack of experimental data to inform the search for parameters as well as to validate the resulting simulations. Recent developments, such as photo bleaching and super high resolution imaging (Ball et al., 2012) are starting to provide this data. Detailed information on features such as 3D cell geometry, reactant concentrations, and reactant locations are providing a basis for this parameter search.

The conversion of experimental data into simulation parameters can prove quite challenging in terms of setting up the *in silico* initial conditions: it is difficult to specify three-dimensional shapes and distributions in an intuitive way. One approach is to use image processing algorithms to extract qualitative features from microscopy images and videos at the same time as noise-reduction algorithms are applied. As an example, PhenoPlot (Sailem et al., 2015) enables the automatic, accurate translation of high resolution microscopy images of cells to convenient glyph based representations of the cell in terms of features such as nuclear texture and size, degree of roundedness, etc. These features can then be used to tailor the characteristics of the virtual cell to be simulated using ReDi-Cell. Thus, with these combined techniques the simulation of more realistic systems within an integrated experimental/computational cycle becomes feasible.

One avenue of further work would investigate how the ratio and distribution of clutter within the cytosol changes the dynamics of cellular pathways.

Another interesting and challenging direction for future work is the understanding the effect of *changing* cell morphology on the dynamics of a biological process. Many real cells exhibit plasticity during their life cycle, changing from one shape to another in order to best suit their environment (Yin et al., 2014). Such changes can be caused by a variety of environmental factors (Young, 2006) with time-scales and degrees of plasticity of varying magnitudes. For example, small shape changes can be seen in most cells due to instabilities in cytoskeletal structure (Kueh and Mitchison, 2009) with larger changes occurring in scenarios such as stem cell differentiation. Nutritional stress is another example of a shape changing factor, causing cells to undergo filamentation (Young, 2007). As seen in Section 6.6, our experiments indicate that filamentation alters the time between external stimulus and internal state change, as the signal has further to travel. Macroscopic behaviour, such as motility, may be altered in interesting ways by this timing change. For example, we know that *Escherichia coli* motor direction switches between two states, forward and tumble (Darnton et al., 2007), due to environmental cues. We are currently performing simulations using ReDi-Cell to answer the question of whether filamentation of *E. coli* alters the time between external stimulus and motility state change, and if this change may account for a widening of the bacteria's search area.

We believe that ReDi-Cell can play a role in the advanced understanding of these complex cellular phenomena. ReDi-Cell can be used to rapidly validate models of how behaviour is modulated by subtle spatial properties such as the shape and size of cells. We expect that further advances in experimental techniques will provide a rich and extensive source of data, and simulation techniques such as ours will provide the necessary tools to make sense of this explosion of data in truly understanding the complex yet elegant functioning of cells.

Acknowledgements

We are grateful for financial support from EPSRC, under grants EP/J500586/1 and EP/I03157X/1(ROADBLOCK: Towards Programmable Defensive Bacterial Coatings and Skins).

Appendix A. The effect of geometry on the Turing system

In this section we show the impact of introducing clutter on a Turing system. Here the single piece of clutter causes discontinuities in the generated pattern.

Fig. A.16

Appendix B. Normalised scale heatmaps

In this section we reproduce the heatmaps found in Fig. 12 with normalised heatmap scales.

Fig. B.17

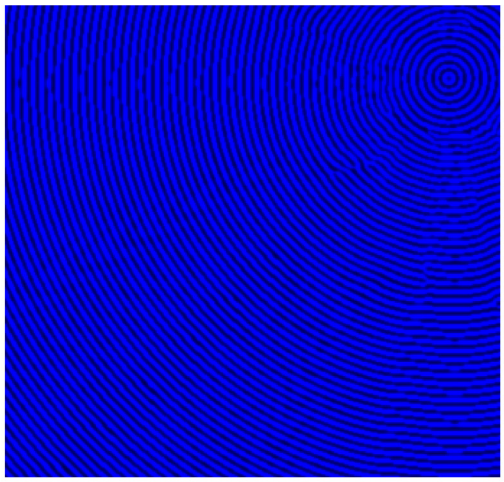

(a) Concentration of Species V in an uncluttered environment

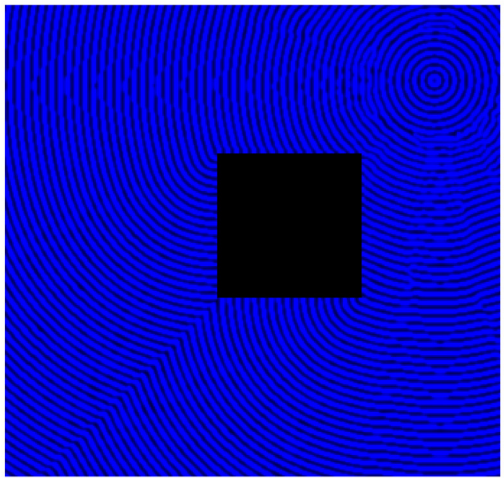

(b) Concentration of Species V in a cluttered environment

Fig. A.16. Concentration map of species V in a turing system after 10000 time steps. The concentration of species V is proportional to the brightness of the blue. $a_u = 0.08$, $b_u = -0.08$, $c_u = 0.04$, $d_u = 0.03$, *reaction rate*$_u = 10^{12}$, $D_u = 0.02$, $a_v = 0.1$, $b_v = 0.0$, $c_v = -0.15$, $d_v = 0.08$, *reaction rate*$_v = 10^{12}$, $D_v = 0.5$

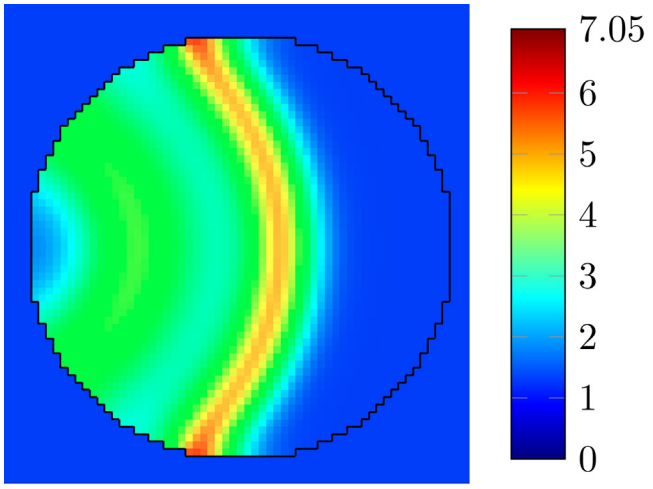

(a) Concentration of Species B in a *Coccus*

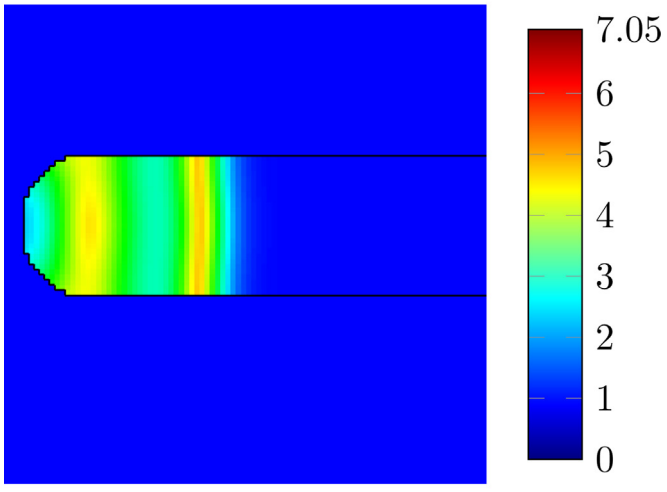

(b) Concentration of Species B in a *Bacillus*

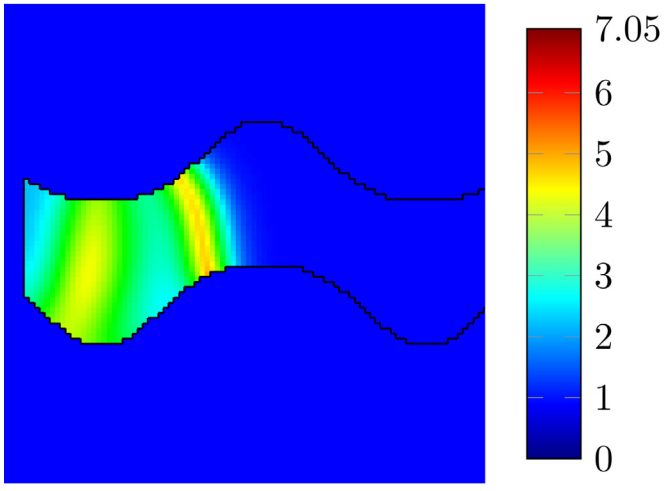

(c) Concentration of Species B in a *Spirillum*

Fig. B.17. LVD wavefronts in natural cell shapes after 1000 time steps. $\alpha = 1.5$, $\beta = 1.0$, $\gamma = 3.0$, $\delta = 1.0$, $\Delta t = 10^{-14}$ s, $\Delta x = 1.0 * 10^{-6}$ m, *reaction rate* $= 10^{12}$, $D = 1.0$

Appendix C. Choice of diffusion coefficients

The value of the diffusion coefficient for a chemical species can dramatically alter the behaviour of the reaction–diffusion system associated with it. Despite the difficulty in measuring diffusion coefficients *some* values of biologically relevant entities have been recorded in the literature; a compilation of common cellular chemicals with their diffusion coefficients can be found in (Milo and Phillips, 2015). Cellular diffusion coefficients are proportional to both the mass of the species and to the density of the medium through which they travel, resulting in a wide range of values. For example in the data in (Milo and Phillips, 2015) diffusion coefficients range from 7000 $\mu m^2/s$ for H^+ ions to 0.001 $\mu m^2/s$ for mRNA. Diffusion coefficients for protein translocation within the cytoplasm have been measured in *E. coli* to be between 30 $\mu m^2/s$ and 0.03 $\mu m^2/s$. In this work we simulate abstracted signalling and metabolic pathways both of which can involve proteins of varying size; with this in mind we choose diffusion coefficients of 1 and 0.1 representing values in-between the minimum and maximum orders of magnitude for protein diffusion. These values represent biologically realistic diffusion coefficients for the types of systems that we are interested in exploring. We reproduce a portion of the diffusion coefficients reported in (Milo and Phillips, 2015) in Table C.5.

Table C.5
Table of diffusion coefficients representative of cellular environments. Reproduced from (Milo and Phillips, 2015).

Molecule	Medium	Diffusion coefficient ($\mu m^2/s$)
H^+	Water	7000
H_2O	Nucleus of Chicken Erythrocyte	200
Protein (≈30 kDa GFP)	eukaryotic cell (CHO) cytoplasm	30
Protein (≈30 kDa)	*E. coli* cytoplasm	7–8
Morphogen (bicod-GFP)	*D. melanogaster* embryo cytoplasm	7
Protein (≈40 kDa)	*E. coli* cytoplasm	2–4
Protein (≈70–250 kDa)	*E. coli* cytoplasm	0.4–0.2
Protein (≈140 kDa Tar-YFP)	*E. coli* cytoplasm	0.2
Protein (≈70 kDa LacY-YFP)	*E. coli* cytoplasm	0.03
mRNA	various locations	0.005–0.001

References

Andrews, S.S., Dinh, T., Arkin, A.P., 2009. Stochastic models of biological processes. In: Encyclopedia of Complexity and Systems Science. Springer, pp. 8730–8749.
Bacterial Shapes, http://microbeonline.com/characteristics-shape-of-pathogenic-bacteria/ (Accessed 05.09.14).
Ball, G., Parton, R.M., Hamilton, R.S., Davis, I., 2012. A cell biologist's guide to high resolution imaging. Methods Enzymol. 504, 29–55.
Blagodatski, A., Sergeev, A., Kryuchkov, M., Lopatina, Y., Katanaev, V.L., 2015. Diverse set of turing nanopatterns coat corneae across insect lineages. Proc. Natl. Acad. Sci. U. S. A. 112 (34), 10750–10755, http://dx.doi.org/10.1073/pnas.1505748112.
Chen, X., Guo, L., Kang, J., Huo, Y., Wang, S., Tan, W., 2014. Calcium waves initiating from the anomalous subdiffusive calcium sparks. J. R. Soc. Interface 11 (91), 20130934.
Childs, H., Brugger, E., Whitlock, B., Meredith, J., Ahern, S., Pugmire, D., Biagas, K., Miller, M., Harrison, C., Weber, G.H., Krishnan, H., Fogal, T., Sanderson, A., Garth, C., Bethel, E.W., Camp, D., Rübel, O., Durant, M., Favre, J.M., Navrátil, P., 2012. VisIt: an end-user tool for visualizing and analyzing very large data. In: High Performance Visualization-Enabling Extreme-Scale Scientific Insight, pp. 357–372.
CUDA, http://www.nvidia.co.uk/object/cuda-parallel-computing-uk.html (Accessed 05.09.14).
Darnton, N.C., Turner, L., Rojevsky, S., Berg, H.C., 2007. On torque and tumbling in swimming *Escherichia coli*. J. Bacteriol. 189 (5), 1756–1764.
den Breems, N.Y., Nguyen, L.K., Kulasiri, D., 2014. Integrated signaling pathway and gene expression regulatory model to dissect dynamics of *Escherichia coli* challenged mammary epithelial cells. BioSystems 126C, 27–40.
Dolcet, X., Llobet, D., Pallares, J., Matias-Guiu, X., 2005. NF-kB in development and progression of human cancer. Virchows Arch. 446, 475–482.
Erban, R., Chapman, J., Maini, P. A practical guide to stochastic simulations of reaction–diffusion processes. arXivarXiv:0704.1908v2.
Eungdamrong, N.J., Iyengar, R., 2004. Computational approaches for modeling regulatory cellular networks. Trends Cell Biol. 14 (12), 661–669.

Fuller, B.G., Lampson, M.A., Foley, E.A., Rosasco-Nitcher, S., Le, K.V., Tobelmann, P., Brautigan, D.L., Stukenberg, P.T., Kapoor, T.M., 2008. Midzone activation of aurora B in anaphase produces an intracellular phosphorylation gradient. Nature 453 (7198), 1132–1136.
Gong, H., Zuliani, P., Komuravelli, A., Faeder, J.R., Clarke, E.M., 2010. Analysis and verification of the HMGB1 signaling pathway. BMC Bioinform. 11 (Suppl 7), S10, Suppl 7.
Hastings, A., 1978. Global stability in Lotka–Volterra systems with diffusion. J. Math. Biol. 6 (2), 163–168.
Howard, M., 2006. Cell signalling: changing shape changes the signal. Curr. Biol. 16 (17), R673-5.
Hwang, Y., Kumar, P., Barakat, A.I., 2014. Intracellular regulation of cell signaling cascades: how location makes a difference. J. Math. Biol. 69 (1), 213–242.
Karr, J.R., Sanghvi, J.C., Macklin, D.N., Gutschow, M.V., Jacobs, J.M., Bolival, B., Assad-Garcia, N., Glass, J.I., Covert, M.W., 2012. A whole-cell computational model predicts phenotype from genotype. Cell 150, 389–401.
Kholodenko, B.N., Kolch, W., 2008. Giving space to cell signaling. Cell 133 (4), 566–567.
Kholodenko, B.N., 2009. Spatially distributed cell signalling. FEBS Lett. 583 (24), 4006–4012.
Kueh, H.Y., Mitchison, T.J., 2009. Structural plasticity in actin and tubulin polymer dynamics. Science 325 (5943), 960–963.
Loew, L.M., Schaff, J.C., 2001. The Virtual Cell: a software environment for computational cell biology. Trends Biotechnol. 19 (10), 401–406.
Lotka, A.J., 1925. Elements of Physical Biology.
Maeder, C.I., Hink, M.A., Kinkhabwala, A., Mayr, R., Bastiaens, P.I.H., Knop, M., 2007. Spatial regulation of Fus3 MAP kinase activity through a reaction–diffusion mechanism in yeast pheromone signalling. Nat. Cell Biol. 9 (11), 1319–1326.
Maini, P., Painter, K., Chau, H.P., 1997. Spatial pattern formation in chemical and biological systems, Journal of the Chemical Society. Faraday Trans. 93 (20), 3601–3610.
Matlab, choosing a solver, https://uk.mathworks.com/help/simulink/ug/types-of-solvers.html (Accessed 29.02.16).
McLaughlin, J.F., Roughgarden, J., 1991. Pattern and stability in predator–prey communities: how diffusion in spatially variable environments affects the Lotka–Volterra model. Theor. Popul. Biol. 40 (2), 148–172, http://dx.doi.org/10.1016/0040-5809(91)90051-G.
Meyers, J., Craig, J., Odde, D.J., 2006. Potential for control of signaling pathways via cell size and shape. Curr. Biol. 16 (17), 1685–1693.
Meyers, R., 2012. Epigenetic Regulation and Epigenomics: Advances in Molecular Biology and Medicine. Wiley-Blackwell, URL https://books.google.co.uk/books?id=jzU7wpL0I40C.
Milo, R., Phillips, R., 2015. Cell Biology by the Numbers. Garland Press, pp. 239, ISBN 9780815345374, See http://www.garlandscience.com/product/isbn/9780815345374.
Modelica, http://blog.xogeny.com/blog/eqs-to-comps-2/ (Accessed 05.09.14).
Neves, S.R., Iyengar, R., 2009. Models of spatially restricted biochemical reaction systems. J. Biol. Chem. 284 (9), 5445–5449.
Niethammer, P., Bastiaens, P., Karsenti, E., 2004. Stathmin–tubulin interaction gradients in motile and mitotic cells. Science 303 (5665), 1862–1866.
Orton, R.J., Sturm, O.E., Vyshemirsky, V., Calder, M., Gilbert, D.R., Kolch, W., 2005. Computational modelling of the receptor-tyrosine-kinase-activated MAPK pathway. Biochem. J. 392 (Pt 2), 249–261, http://dx.doi.org/10.1042/BJ20050908.
Plimpton, S.J., Slepoy, A., 2005. Microbial cell modeling via reacting diffusive particles. In: J. Phys.: Conf. Ser, p. 305.
Press, W.H., Teukolsky, S.A., Vetterling, W.T., Flannery, B.P., 2002. Numerical Methods in C++, 3rd ed. Cambridge University Press.
Sailem, H.Z., Sero, J.E., Bakal, C., 2015. Visualizing cellular imaging data using PhenoPlot. Nat. Commun. 6, 5825.
Smith, G.D., 1985. Numerical Solutions of Partial Differential Equations: Finite Difference Methods, 3rd ed. OUP, Oxford.
Soh, S., Byrska, M., Kandere-Grzybowska, K., Grzybowski, B.A., 2010. Reaction–diffusion systems in intracellular molecular transport and control. Angew. Chem. Int. Ed. 49 (25), 4170–4198.
Srere, P.A., 2000. Macromolecular interactions: tracing the roots. Trends Biochem. Sci. 25, 150–153.
Turing, A., 1990. The chemical basis of morphogenesis. Bull. Math. Biol. 52 (1–2), 153–197, http://dx.doi.org/10.1007/BF02459572.
Volterra, V., 1927. Variazioni e fluttuazioni del numero d'individui in specie animali conviventi.
Weng, G., Bhalla, U.S., Iyengar, R., 1999. Complexity in biological signaling systems. Science 284 (5411), 92–96.
Yin, Z., Sailem, H., Sero, J., Ardy, R., Wong, S.T.C., Bakal, C., 2014. How cells explore shape space: a quantitative statistical perspective of cellular morphogenesis. Bioessays 36 (12), 1195–1203.
Young, K.D., 2006. The selective value of bacterial shape. Microbiol. Mol. Biol. Rev. 70 (3), 660–703.
Young, K.D., 2007. Bacterial morphology: why have different shapes? Curr. Opin. Microbiol. 10 (6), 596–600.
Zhao, Q., Yi, M., Liu, Y., 2011. Spatial distribution and dose–response relationship for different operation modes in a reaction–diffusion model of the MAPK cascade. Phys. Biol. 8 (5), 055004.